Increased Aggregation Tendency of Alpha-Synuclein in a Fully Disordered Protein Complex

David A. Merle[1,9], Anja Witternigg[1], Carmen Tam-Amersdorfer[2], Christoph Hartlmüller[3,4], Emil Spreitzer[5], Evelyne Schrank[1], Sabine Wagner-Lichtenegger[6], Oliver Werzer[7], Klaus Zangger[1], Andreas J. Kungl[7], Tobias Madl[5], N. Helge Meyer[8] and S. Fabio Falsone[7]

1 - Institute of Chemistry, *University of Graz, Heinrichstr. 28, 8010 Graz, Austria*
2 - Otto Loewi Research Center for Vascular Biology, *Immunology and Inflammation, Institute of Pathophysiology and Immunology, Medical University of Graz, Heinrichstr, 31, 8010 Graz, Austria*
3 - Center for Integrated Protein Science Munich (CIPSM) at the Department of Chemistry Technische Universität München, *Lichtenbergstr. 4, 87548, Garching, Germany*
4 - Institute of Structural Biology, *Helmholtz Zentrum München, Ingolstädter Landstraße 1, 85764 Neuherberg, Germany*
5 - Gottfried Schatz Research Center for Cell Signaling, *Metabolism and Aging, Institute of Molecular Biology & Biochemistry, Medical University of Graz, Neue Stiftingtalstrasse 6, 8010 Graz, Austria*
6 - Diagnostic & Research Center for Molecular BioMedicine, *Institute of Hygiene, Microbiology and Environmental Medicine, Medical University Graz, Neue Stiftingtalstraße 2, 8010 Graz, Austria*
7 - Institute of Pharmaceutical Sciences, *University of Graz, Schubertstr. 1, 8010 Graz, Austria*
8 - Division of Experimental Allergology and Immunodermatology, *Department of Human Medicine, University of Oldenburg, Carl-von-Ossietzky-Straße 9-11, 26129 Oldenburg, Germany*

Correspondence to Tobias Madl, N. Helge Meyer and S. Fabio Falsone: *tobias.madl@medunigraz.at, helge.meyer@uni-oldenburg.de, fabio.falsone@uni-graz.at.*
https://doi.org/10.1016/j.jmb.2019.04.031
Edited by Monika Fuxreiter

Abstract

The recent discovery of biologically active fully disordered, so called random fuzzy protein–protein interactions leads to the question of how the high flexibility of these protein complexes correlates to aggregation and pathologic misfolding.

We identify the structural mechanism by which a random fuzzy protein complex composed of the intrinsically disordered proteins alpha-Synuclein and SERF1a is able to potentiate cytotoxic aggregation. A structural model derived from an integrated NMR/SAXS analysis of the reconstituted aSyn:SERF1a complex enabled us to observe the partial deprotection of one precise aSyn amyloid nucleation element in the fully unstructured ensemble. This minimal exposure was sufficient to increase the amyloidogenic tendency of SERF1a-bound aSyn.

Our findings provide a structural explanation of the previously observed pro-amyloid activity of SERF1a. They further demonstrate that random fuzziness can trigger a structurally organized disease-associated reaction such as amyloid polymerization.

Introduction

Fuzzy protein complexes that involve intrinsic protein disorder can assume many biological functions [1]. In the extreme case - referred to as random fuzziness - protein–protein interactions can even be mediated without any formation of a stable three-dimensional structure [2]. This functional mode of molecular recognition between intrinsically disordered proteins (IDPs) is in sharp contradiction to the traditional structure–function paradigm, which states that polypeptides underlie a strict folding hierarchy for a precise biological process. Yet, structural disorder generally increases the probability of a

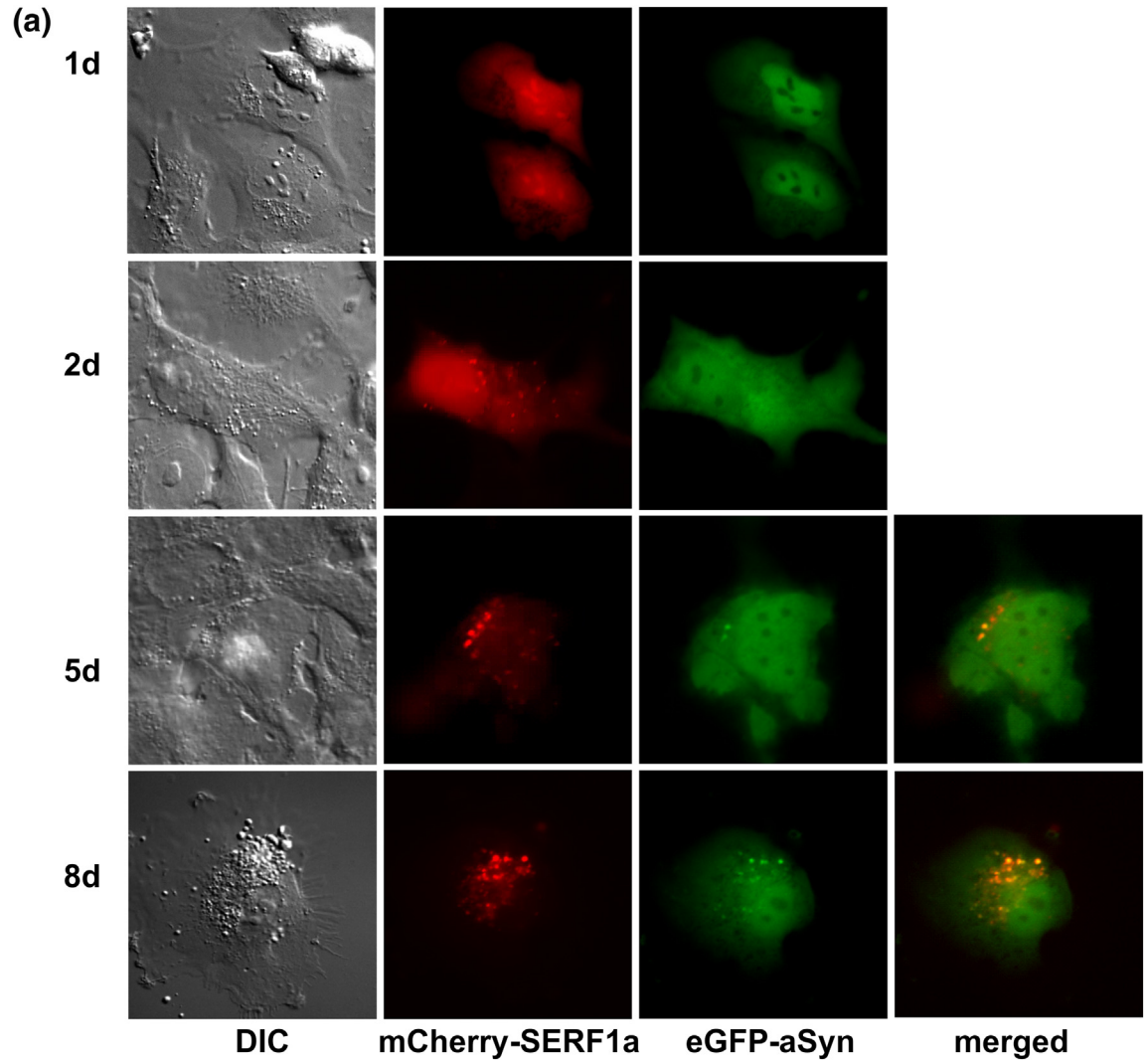

Fig. 1. aSyn and SERF1a interact directly in the cell. (A) living cell fluorescence microscopy images of SH-SY5Y neuroblastoma cells co-transfected with mCherry-SERF1a (red) and eGFP-aSyn (green). Merged images highlight co-localization (yellow). Time captions indicate days (d) after co-transfection. Left panels: corresponding differential interference contrast (DIC) images. (B) Representative immunofluorescence microscopy images of two distinct regions of cortical tissue from paraffin embedded 2 months old C57BL/6 mouse brain sections. White arrows indicate co-localization of SERF1a (green) and aSyn (red) to punctate foci (yellow). Immunofluorescence controls in the absence of dye-conjugated secondary antibodies are shown directly below. See also Fig. S1D. (C) ThS staining of the corresponding brain region is negative, attesting the absence of amyloid particles. (D) living cell fluorescence microscopy images of SH-SY5Y neuroblastoma cells co-transfected with the SERF1a point mutant mCherry-K17E(red) and eGFP-aSyn (green). Time caption indicates days (d) after co-transfection. Left panel: corresponding differential interference contrast (DIC) image. (E) Co-immunoprecipitation of an endogenous aSyn:SERF1a complex from healthy mouse brain extracts by SERF1a-directed antibody (IP). First lane: no antibody (Ab) control; second lane: pull-down under low ionic strength conditions (50 mM NaCl); third lane: pull-down under physiologic ionic strength conditions (150 mM NaCl). Proteins were detected by immunoblotting (IB).

polypeptide chain to acquire functionally undesired, *i.e.* misfolded conformations with toxic properties [3]. Indeed, a high degree of conformational freedom facilitates protein misfolding, functional deterioration, and finally disease. Considering that fuzzy protein complexes do not undergo hydrophobic collapse, one question arising is how these high levels of structural disorder correlate to protein misfolding and aggregation.

Here, we describe that a fuzzy interaction between the intrinsically disordered protein pair SERF1a (a member of the Modifier of aggregation-4/Small EDRK-rich factor (MOAG-4/SERF) family) and alpha synuclein (aSyn) generates an entirely disordered protein complex with an increased tendency to amyloid aggregation. In eukaryotes, MOAG-4/SERF selectively modifies the amyloid polymerization of

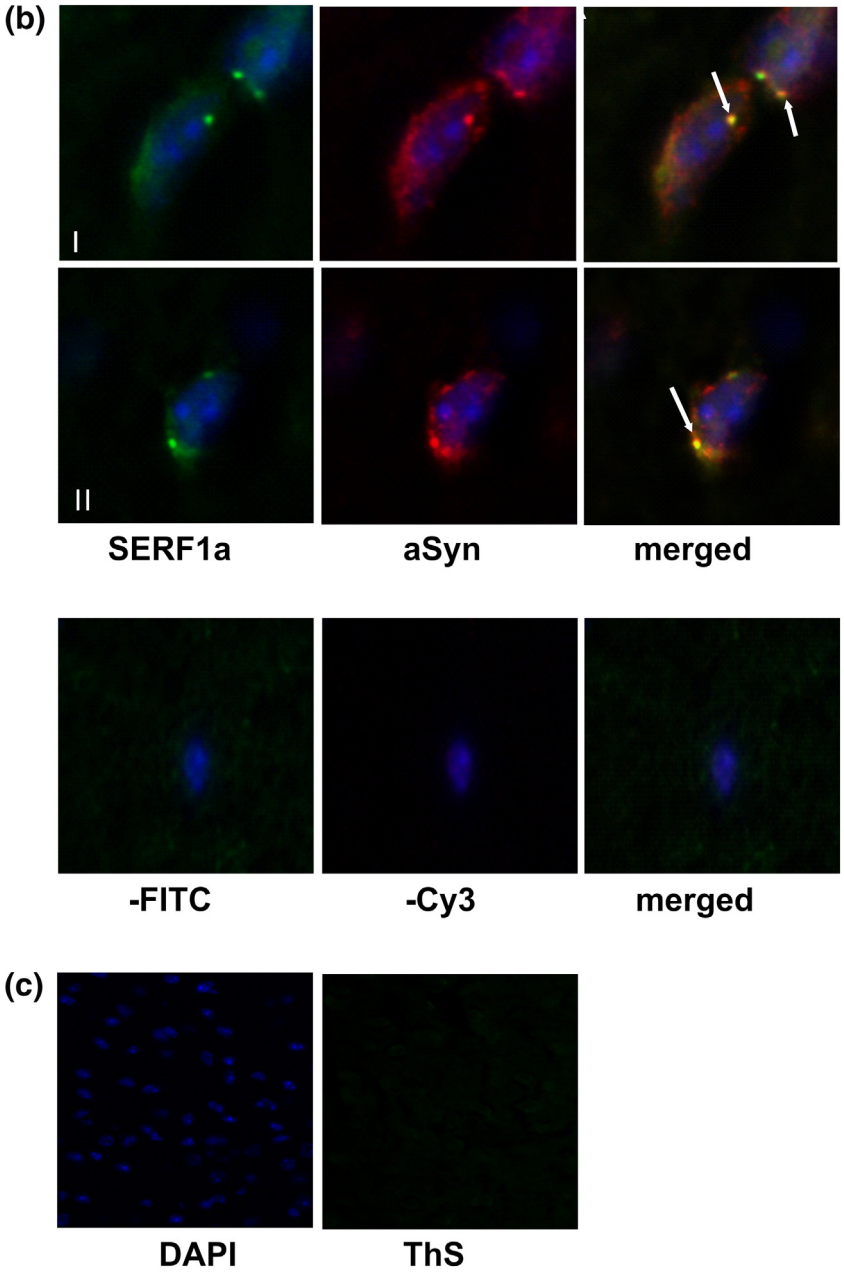

Fig. 1. (*continued*).

interacting proteins such as aSyn [4,5]. While the overexpression of MOAG-4/SERF promotes the misfolding of aSyn and of other amyloidogenic proteins into cytototoxic species, a downregulation is cytoprotective and acts against cellular aging [4]. In neurons, aSyn controls the assembly of presynaptic vesicles required for the release of the neurotransmitter dopamine [6]. The aggregation of aSyn into intracellular amyloid inclusions known as Lewy Bodies coincides with the death of dopaminergic neurons, and therefore constitutes a pathologic signature of synucleinopathies such as Parkinson's disease, dementia with Lewy bodies, and multiple system atrophy [7]. Consequently, MOAG-4/SERF proteins have been linked to neuronal aSyn toxicity.

Although the interaction with SERF1a is sufficient to trigger the production of “on-amyloid pathway” aSyn nucleation seeds [5], the structural details of this harmful amyloidogenic process have remained unsolved.

By the integrated use of nuclear magnetic resonance spectroscopy (NMR) and small angle X-ray scattering (SAXS), we analyze the structural mechanism underlying SERF1a-regulated amyloidogenesis. We show that a) SERF1a and aSyn retain their

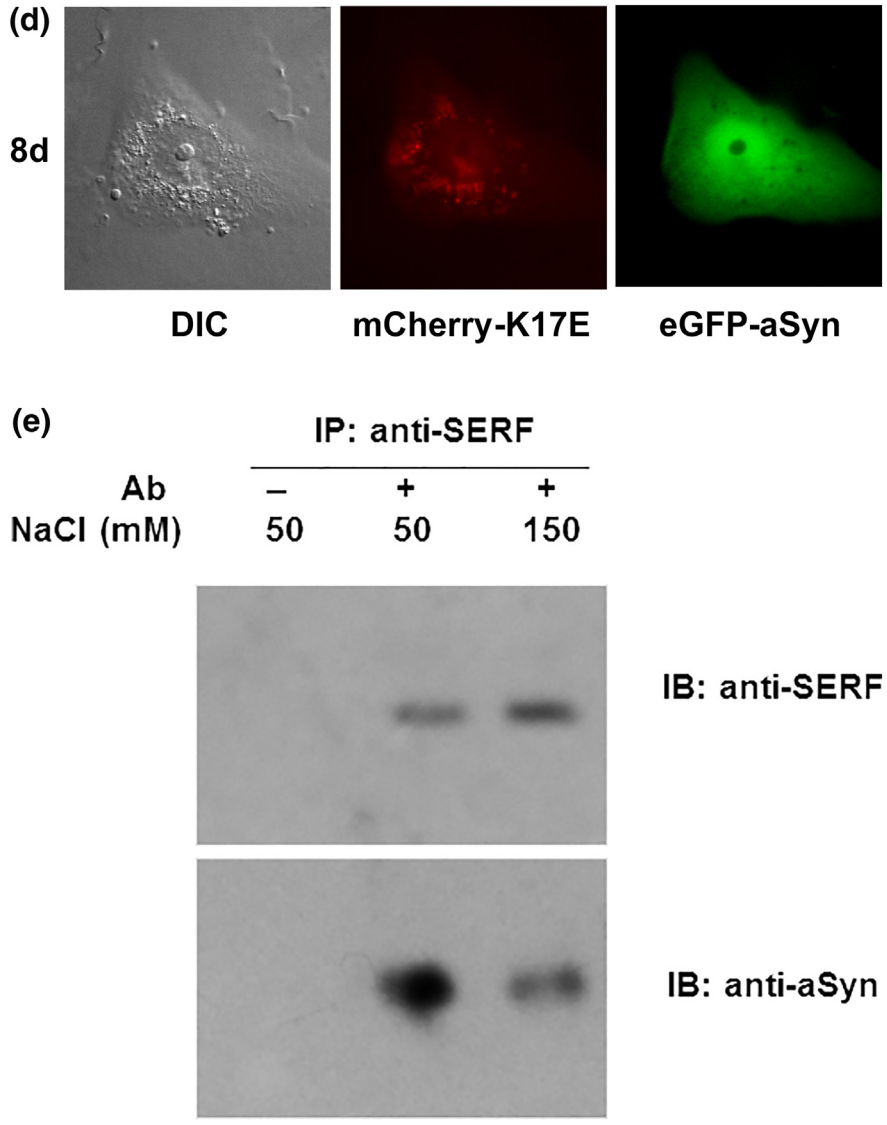

Fig. 1. (*continued*).

intrinsically disordered state to form a highly dynamic structural ensemble, b) the interaction is purely electrostatic, and c) the aggregation tendency of SERF1a-bound aSyn is increased by the limited deprotection of one specific amyloid nucleation element.

These results establish that fuzzy complexes can prime a proteotoxic reaction such as amyloid self-assembly without the explicit induction of stable structure.

Results

The aSyn:SERF1a interaction is transient and locally delimited in the cell

The existence of a direct protein–protein interaction between SERF1a and aSyn *in vivo* has remained undetectable so far. We hypothesized that this was due to their transient association shown *in vitro* [5]. We used protein overexpression in SHSY-5Y neuroblastoma cells to analyze the distribution of *SERF1a* and *aSyn* fused to the fluorescence tags mCherry and eGFP, respectively (Fig. 1A. See Fig. S1A and Fig. S1B for the corresponding single transfection controls). One day after transfection, we observed a SERF1a signal in the nucleus, in nucleoli, as well as diffusely in the cytosol. This indicated that SERF1a was able to partition between various compartments. Two days after transfection, we noticed an incipient intracellular redistribution from the nucleus to the cytosol. Within 5 days, the SERF1a fluorescence progressively disappeared from nuclei and nucleoli, while gradually increasing in initially absent punctate

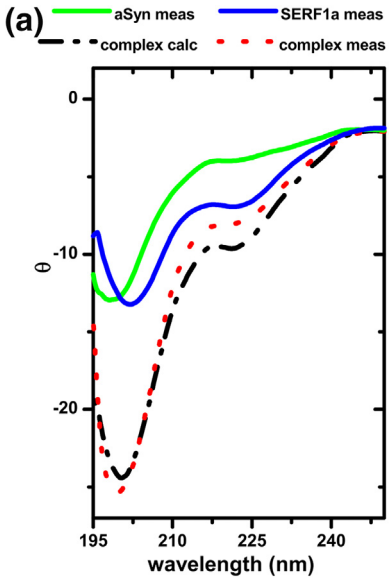

Fig. 2. absence of secondary structure in the aSyn:SERF1a complex. (A) Experimental far-UV CD-curves of aSyn (solid green line), SERF1a (solid blue line), and of an equimolar mixture of aSyn and SERF1a (dashed red line). Single spectra of aSyn and SERF1a show patterns of conformational disorder (lack of predominant minima at 222 nm and 208 nm (alpha-helix), or at 216 nm (beta sheet)), and a strong negative signal with slow positive recovery below 205 nm. A calculated spectrum of the aSyn:SERF1a complex (dash-dotted black curve), obtained by the addition of single experimental aSyn and SERF1a spectra, shows a similar profile to the empirically measured spectrum of the aSyn:SERF1a complex. (B) $13C^{\alpha/\beta}$ secondary chemical shifts (upper panel) and $\{^1H\}$-^{15}N heteronuclear NOE values (lower panel) of SERF1a either free (black) or in complex with aSyn (red). (C) $13C^{\alpha/\beta}$ secondary chemical shifts (upper panel) and $\{^1H\}$-^{15}N heteronuclear NOE values (lower panel) of aSyn either free (black) or in complex with SERF1a (red).

cytosolic bodies. Interestingly, the aSyn and the SERF1a fluorescence signals started to distinctly overlap within these puncta after approximately 5 days, suggesting an incorporation of aSyn subsequent to that of SERF1a. The distribution of aSyn remained randomly diffuse in cells which did not overexpress SERF1a (Fig. S1B), suggesting a causal relationship for the stepwise accumulation of SERF1a and aSyn into cytosolic bodies. Surprisingly, the late co-localization pattern observed in transfected neuroblastoma cells after 8 days was closely similar to that of endogenous aSyn and SERF1a in healthy mouse brain tissue, where both proteins could be detected by immunofluorescence staining (Fig. 1B and Fig. S1D). This was particularly evident in cells from fixed cortical sections, where the protein fluorescence signals appeared diffusely in the cytosol, as well as overlapping in well-defined cytosolic puncta, in close analogy to transfected living cells. As these cytosolic bodies resulted negative to the amyloid-staining dye Thioflavin S (Fig. 1C), we deduced that aSyn was non-amyloid, which corroborates *in vitro* findings of SERF1a associating exclusively with non-aggregated aSyn.

We anticipate (see *the aSyn:SERF1a interaction is driven by charge*) that mutations disrupting the interaction between aSyn and SERF1a *in vitro* abolished cellular co-localization in cytosolic bodies (Fig. 1D. See Fig. S1C for the corresponding single transfection control), suggesting a direct association of both molecules also *in vivo*. We confirmed direct binding by immunocapturing of an aSyn:SERF1a complex out of mouse brain homogenates (Fig. 1E). The association was favored by low ionic strength conditions (50 mM NaCl), while being weaker, but still detectable at physiologic strength (150 mM), indicating a significant charge contribution for the interaction.

Collectively, these results point to a direct, weak, charge- and time-dependent interaction which is locally delimited to punctate cytosolic compartments, consistent to the previously observed transient character of the isolated *in vitro* complex [5].

aSyn and SERF1a remain intrinsically disordered in complex

To understand the molecular principles of such transient interaction, aSyn and SERF1a were purified and the reconstituted complex was biophysically analyzed *in vitro*. Disorder-to-order transitions are very common for IDPs [8] or proteins containing intrinsically disordered regions (IDRs), and they are a structural prerequisite of aSyn amyloidogenesis [9]. As SERF1a and aSyn are both intrinsically disordered [5,10], we initially hypothesized that their association might lead to the formation of a well-structured scaffold that facilitates amyloid formation.

We qualitatively assessed bulk conformational changes by circular dichroism (CD) spectroscopy, which can reveal secondary structure rearrangements of polypeptides in solution. Notably, the CD spectrum of the reconstituted aSyn:SERF1a complex was similar to the linear combination of the individual aSyn and SERF1a spectra (Fig. 2A). Moreover, a strongly negative signal diagnostic of random coils [11] prevailed in the spectrum of the complex below 205 nm. These results suggest the absence of folding upon binding, and the highly atypical persistence of structural disorder even in complex.

We used NMR spectroscopy to analyze the unexpectedly high conformational flexibility of the aSyn:SERF1a complex in more detail at atomic resolution. In particular, we used i) $^{13}C^{\alpha}$ and $^{13}C^{\beta}$ (13Cα/β) secondary chemical shifts to identify the folding propensity [12,13], and ii) $\{^1H\}$-^{15}N

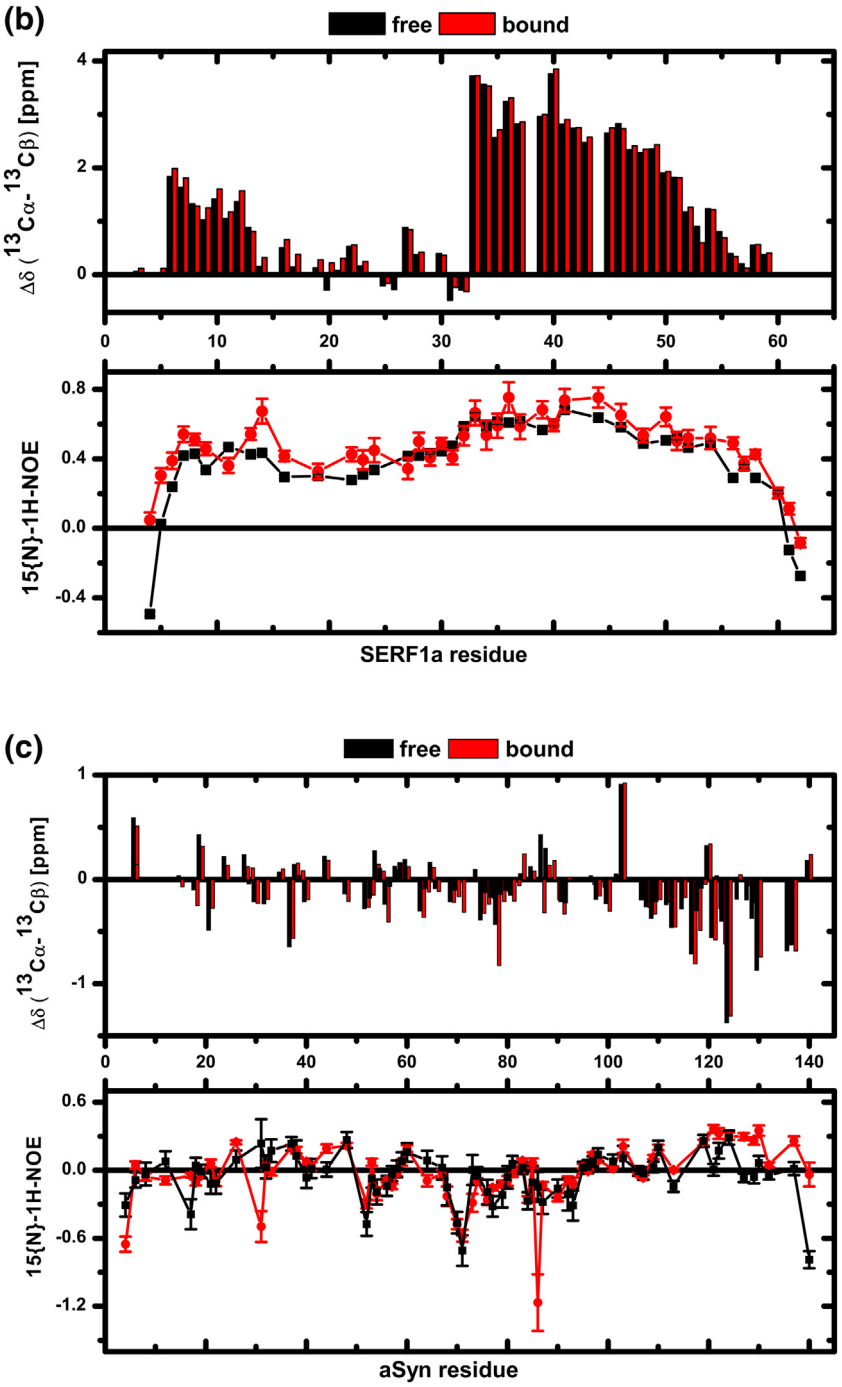

Fig. 2. (*continued*).

heteronuclear Nuclear Overhauser Effects (NOEs) [14] to assess the backbone flexibility of the two proteins free and in complex.

From 13Cα/β secondary chemical shifts, we found that the free form of SERF1a contains a short N-terminal (aa 5–15) and a long C-terminal segment (aa 35–60) which are predisposed to adopt an alpha-helical conformation (Fig. 2B, upper panel), in agreement with *in silico* secondary structure predictions (Fig. 3A). However, these helices are only minor populated in unbound SERF1a, as characteristic NOE patterns are not observable (data not shown). In addition, an average $\{^{1}H\}$-^{15}N NOE value of 0.39 ± 0.23 (Fig. 2B, lower panel) indicates an overall flexibility of the SERF1a backbone. The results coincide with structural data from the *C.*

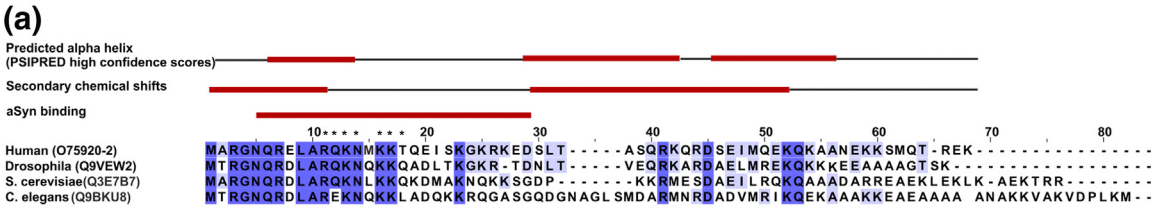

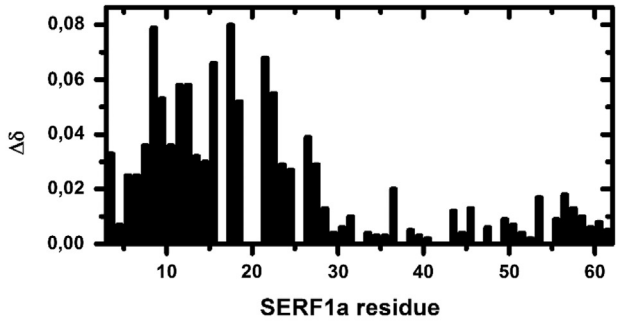

(c)

mutation	K_D-values [μM]
wt	2.56±0.32
R11A	2.52±0.54
R11E	6.54±0.74
Q12A	3.61±0.39
K13A	33.89±8.56
K13E	no saturable binding
N14A	37.78±18.41
K16A	124.91±48.49
K16E	no saturable binding
K17A	83.71±33.88
K17E	no saturable binding
T18A	2.04±0.44
aSynC-pSer129	
wt	0.42±0.03

Fig. 3. influence of charge on the aSyn:SERF1a interaction. (A) Upper scheme, first line: *in silico* structure prediction of human SERF1a. Red: predicted alpha helical regions (PSIPRED confidence score > 6 [50]). Black: predicted low structural complexity. Second line: structural propensity of SERF1a (red: alpha helix) assessed from $13C^{\alpha/\beta}$ secondary chemical shifts. Third line: aSyn binding region (red) derived from ^{1}H,^{15}N-HSQC-NMR chemical shift perturbations. Lower scheme: evolutionary conservation of MOAG/SERF homologs among eukaryotes. Swissprot ID numbers are in brackets. Blue: highly conserved amino acid residues. Pale blue: conserved residues between at least two homologs. Asterisks mark amino acid residues which were selected for mutagenesis. (B) SERF1a ^{1}H,^{15}N-HSQC-NMR perturbation diagram showing chemical shift changes Δδ upon the addition of aSyn. (C) K_D-values obtained by fluorescence anisotropy saturation titrations of a FITC-labeled aSyn C-terminal peptide (aSynC) with wildtype SERF1a (wt) or with selected SERF1a single-point charge variants (see also Fig. S3). Lower table section: K_D-value of wtSERF1a for FITC-labeled aSynC- selectively phosphorylated at Ser129 (aSynC-pSer129). The values are mean averages including S.E.M. of three independent measurements.

elegans orthologue MOAG-4, which displays two similar bipartite segments with alpha-helical tendency and high backbone dynamics [15]. Thus, intrinsic structural disorder and alpha helical folding propensity are conserved features of MOAG-4/SERF family members.

Upon binding to aSyn, there was a slight increase of some SERF1a $\{^{1}H\}$-^{15}N NOEs (Fig. 2B, lower panel), especially within the aSyn binding site (SERF1a residues 10–25. See Fig. 3A and next paragraph). In general, however, values remained below those expected for rigidly folded structure (around 0.8) [14], arguing for a persistent structural flexibility of the SERF1a backbone in complex. Moreover, little 13Cα/β secondary chemical shifts variation between free and bound SERF1a (Fig. 2B, upper panel) suggested that its backbone conformation remained unchanged. We also did not observe folding of regions flanking the interaction site, a process that can influence binding affinity and specificity of intrinsically disordered proteins [16].

For bound aSyn, 13Cα/β secondary chemical shifts of the NAC (non-Abeta component) region (aa 45–96), which constitutes the stable core of aSyn amyloid fibrils [17–20], were decreased and negative signals became more pronounced (Fig. 2C, upper panel), pointing to an increased tendency for extended or beta-sheet structure. Yet, $\{^{1}H\}$-^{15}N NOEs of complexed aSyn remained between −0.5 and 0.4 (Fig. 2C, lower panel), well below those expected for rigid structure, indicating that stable beta-sheet formation did not occur. Similarly, a

{^{1}H}-^{15}N NOE signal of approximately 0.4 indicated that stable folding was absent at the direct SERF1a binding site (C-terminal residues 110–140) [5]. From these results we conclude that SERF1a and aSyn both remain highly unstructured even in complex.

The aSyn:SERF1a interaction is driven by charge

We proceeded to map the binding sites of the aSyn:SERF1a complex. To this end we recorded ^{1}H, ^{15}N HSQC NMR spectra of aSyn and SERF1a, in the absence and in the presence of the complementary partner. Spectra showed only narrow proton signal dispersion around 8.2 ppm in the ^{1}H dimension even in the bound state, confirming the absence of folding upon binding (Fig. S2). From chemical shift titrations of isotope labeled SERF1a with aSyn, we could observe significant chemical shift perturbations (CSPs) localized to an extended N-terminal stretch of amino acids (Fig. 3B). Prominently affected amino acids (>0.05 ppm) resided on an evolutionary conserved, mainly positively charged arginine/lysine rich motif (amino acids 6–28; Fig. 3A), largely coinciding to a region of limited folding propensity and highest structural flexibility (lowest overall {^{1}H}-^{15}N NOE values, 0.3–0.4; amino acids 10–25; Fig. 2B, lower panel). These results define a basic SERF1a region which is electrostatically complementary to the acidic SERF1a binding site at the C-terminus of aSyn [5]. We thus supposed that molecular recognition occurred exclusively by electrostatic interactions at the direct binding site. Fluorescence anisotropy binding titrations between a minimal aSyn binding peptide (aa 111–140; aSynC) and a series of SERF1a mutants showed that, indeed, the highly basic composition of this SERF1a region was essential for complex formation (Fig. 3C and Fig. S3). The modest binding affinities of the aSynC:SERF1a complex - K_D = 2 μM at low ionic strength and 46 μM at physiologic ionic strength (Fig.S3A and Fig. S3N) - reflect the salt dependency of the interaction in brain extracts (see *The aSyn:SERF1a interaction is transient and locally delimited in the cell*). Replacing one single positively charged residue of the binding interface with alanine was sufficient to compromise the affinity of the interaction by various orders of magnitude. Reversal of charge even abrogated binding *in vitro* (*e.g.* K13E, K16E, or K17E mutations). Consistently, co-localization between aSyn and the non-binding SERF1a charge variant K17E (undetectable K_D-value. See Fig. 3C and Fig. S3K) became unobservable. Although K17E distributed to cytosolic bodies in a time-dependent fashion similar to wtSERF1a, the aSyn fluorescence signal remained diffuse, indicating that aSyn did not incorporate into these bodies (Fig. 1D). Notably, these different single charge mutations affected the K_D value to variable extents. R11A did not alter the K_D value despite the removal of one charge, while *e.g.* K13A, K16A and K17A caused a 14-fold, 50-fold, and 33-fold increase, respectively. Moreover, N14A decreased binding by a factor of >10, despite the unmodified positive net charge of the binding region. This suggests that, unlike *e.g.* for positively charged polyamines [21], the binding affinity of SERF1a for aSyn did not simply correlate with the effective number of basic residues. These findings highlight the requirement of a specific residue composition for binding.

The present results consolidate our previous findings of a complete binding inhibition upon the bulk deletion of the acidic C-terminal aSyn tail [5]. In line with this, the attachment of one single negative charge to the acidic aSyn tail, *i.e.* a phosphate group at Ser129 led to a fivefold increase in complex binding affinity (K_D = 420 ± 30 nM) (Fig. 3C and Fig. S3M), suggesting a possible regulation of the binding process by post-translational modifications.

SERF1a causes the partial exposure of one aSyn amyloid nucleation site

As beta-sheets are well-recognized structural blueprints of amyloids, we reasoned that the extended/beta-sheet fold tendency of bound aSyn reflects an increased propensity towards amyloid folding. Moreover, we noticed a significant decrease of {^{1}H}-^{15}N NOEs for two distinct aSyn residues, namely Gly31 and Gly86 (from 0.2 to −0.5 and from −0.2 to −1.2, respectively) (Fig. 2C, lower panel). Both residues are adjacent to two aSyn segments (approx. aa 20–30 and approx. aa 90–100) that contribute to the autoinhibition of amyloidogenesis by undergoing intramolecular long-range shielding contacts [21–23]. We supposed that binding of SERF1a to aSyn might weaken these contacts, which is a recognized trigger of amyloidogenesis in concomitance to aSyn C-terminal ligand binding [21]. In support to this hypothesis, we found that solvent paramagnetic relaxation (sPRE) was generally enhanced for bound aSyn (Fig. S4). This implies a higher accessibility of the soluble paramagnetic agent Gd(DTPA-BMA) to bound Syn, and consequently a higher solvent exposure of aSyn surfaces in complex with SERF1a. In further support, Yoshimura et al. have reported a similar mechanism of action for MOAG-4 [15]. The authors demonstrate that MOAG-4 promotes aSyn aggregation by competing with the protein's self-protective tertiary contacts, thus substantiating a model of SERF1a-induced autoinhibitory contact loosening.

These considerations prompted us to analyze the ensemble structure of the aSyn:SERF1a complex by using an integrated approach where we combined NMR and SAXS data with ensemble modeling [24–26]. Scattering curves recorded for the isolated

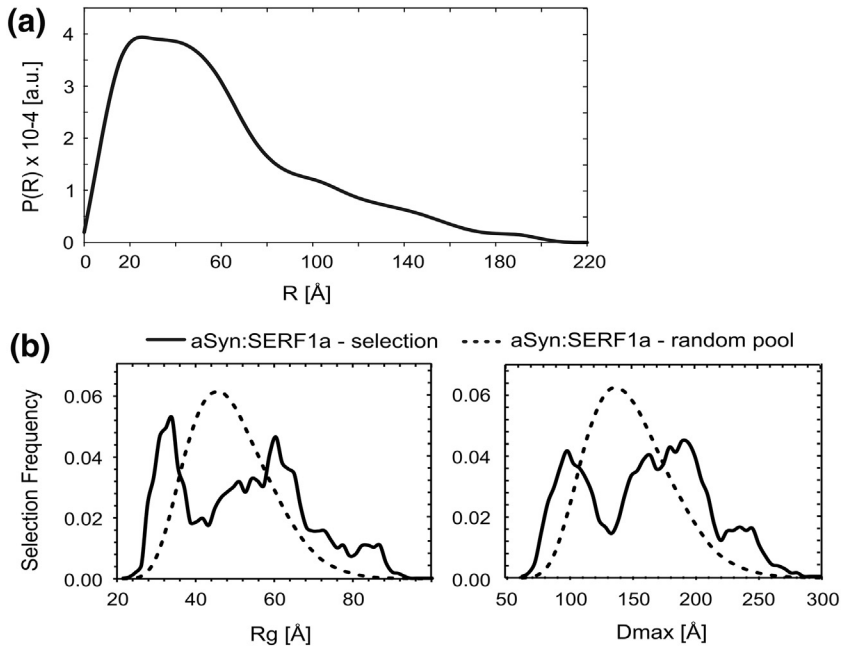

Fig. 4. Overall shape of the aSyn:SERF1a complex. (A) The SAXS-based experimental radial density distribution shows that αSyn and SERF1a form an extended complex. (B) R_g (left) and D_{max} (right) distributions of the EOM models of the αSyn:SERF1a complex in the initial pool of structures with randomized chains (dashed lines) and in the selected ensembles (solid black lines).

proteins showed that SERF1a is monomeric in solution, while aSyn showed a scattering curve characteristic for soluble aggregates (Fig. S5). In complex, SERF1a and aSyn formed a 1:1 stoichiometric complex, as indicated by the disappearance of the scattering signal at low q-ranges characteristic for the strongly scattering soluble aggregates, and the observed molecular weight of 30 kDa (Fig. 4A and Table 1). These results demonstrate that aSyn does not immediately oligomerize in the presence of SERF1a.

To model the structure of the aSyn:SERF1a complex, we first generated a pool of independent structures based on the amino acid sequence and NMR data using the molecular dynamics/simulated annealing program ARIA/CNS [27], and subsequently selected an ensemble of structures that best describes the experimental SAXS data. To generate the pool of structures, we combined complementary sets of NMR data, namely i) backbone dihedral angle restraints, ii) CSPs defining the aSyn:SERF1a binding interface, and iii) distance restraints obtained from paramagnetic relaxation enhancements (PREs) of selectively labeled spin-conjugated proteins (Fig. S6). Although PRE-based distance restraints are well suited to detect long-range interactions in disordered proteins [22,23,28], they provide mainly information on compact conformations of a structural ensemble. Thus, to obtain a pool of extended structures, we initially carried out calculations without PRE-data. The genetic algorithm implemented in the EOM program [24] was then used to select an ensemble of aSyn:SERF1a complex structures that best describes the experimental SAXS data. We identified the best ensemble concerning the agreement of experimental and back-calculated data and compared the R_g and D_{max} distributions of the pool of structures excluding PREs (random pool) to the selected ensembles (Fig. 4B). The selected ensemble shows a higher degree of compaction compared to the random pool. This suggests that there must be inter-domain interactions within the aSyn:SERF1a complex that lead to a non-random compaction.

In order to reveal structural features of these compact conformations, we analyzed pairwise C^{α}-distances in the calculated ensemble, by including

Table 1. SAXS data and analysis. The apparent molecular mass and R_g is shown for αSyn and SERF1a alone and in complex with each other. The molecular mass was determined from the Porod volume.

Sample	R_g [Å]	D_{max} [Å]	Molecular mass [kDa]
αSyn	aggregated	aggregated	aggregated
SERF1a	40.6 ± 4.0	150	17
αSyn:SERF1a (1:1)	48.1 ± 1.6	220	30

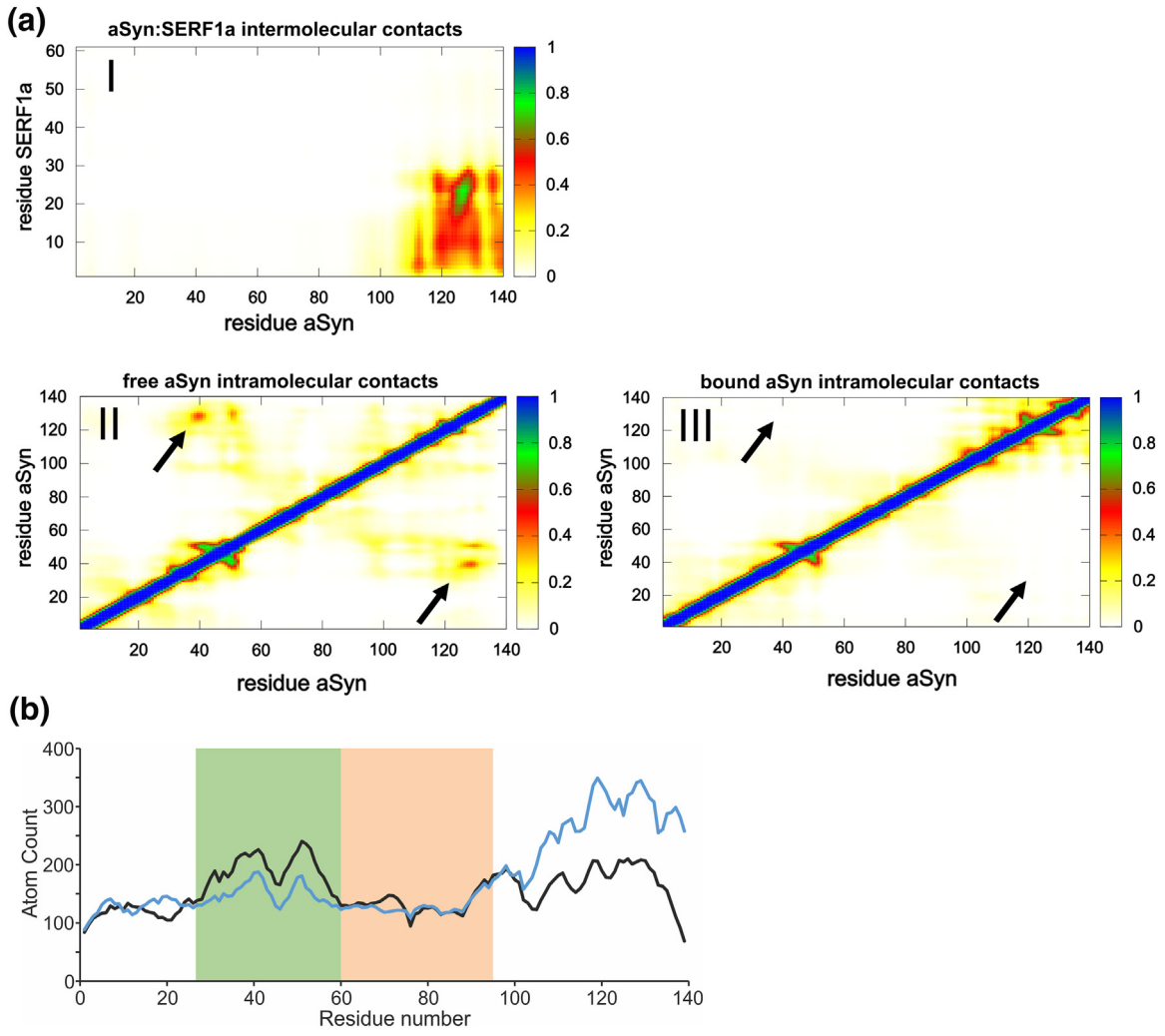

Fig. 5. SERF1a induces the partial exposure of an aSyn amyloidogenic region. (A) intra- and intermolecular contact plot of the aSyn:SERF1a ensemble based on NMR restraints, including distances derived from PREs. Color key shows the fraction of structures with a contact between two given residues (1 corresponds to a contact in all structures of the ensemble). (B) Neighboring heteroatom counting diagram of aSyn ensemble atoms in the absence (black) and presence (blue) of SERF1a as a measure for the averaged degree of exposure. The green area highlights the changes in surface accessibility for amino acid residues 30–60, as well as their partial overlap with the NAC (black mark, aa 45–96). The orange area highlights minimally changed traces for the NAC core (aa 61–96). (C) Structural models of the calculated ensembles (superposition of twenty lowest energy structures) for aSyn (upper panel) and aSyn:SERF1a (lower panel). Coloring scheme: SERF1a, gray; aSyn residues 30–60, green; NAC core region (aa 61–96), orange; remaining aSyn structure, blue). (D) Three-dimensional amyloid structure of an aSyn NAC steric zipper (PDB 6H6B) [18]. Residues 30–60 (green) encompass the preNAC ($_{47}$GVVHGVTTVA$_{56}$), which corresponds to a beta-stranded protofibril-dimerisation interface N-terminal to the NAC beta-sheet amyloid core (aa 61–96, orange).

both intramolecular and intermolecular PRE-based distance restraints (for a detailed overview of the spin-labeled probe combinations, see Fig. S5). A representation of aSyn:SERF1a complex as a contact plot shows the fraction of structures in the ensemble with a specific contact between two residues (Fig. 5A, panel I). In line with NMR titration experiments, stable intermolecular contacts were established between the N-terminus of SERF1a and the C-terminus of aSyn. The absence of additional stable contacts between SERF1a and aSyn also implies the absence of any secondary binding motif.

The intramolecular contact patterns of unbound aSyn (Fig. 5A, panel II) clearly differed from those of SERF1a-bound aSyn (Fig. 5A, panel III). Long-range tertiary contacts between residues 30–60 and 120–140 are typically observed for monomeric aSyn

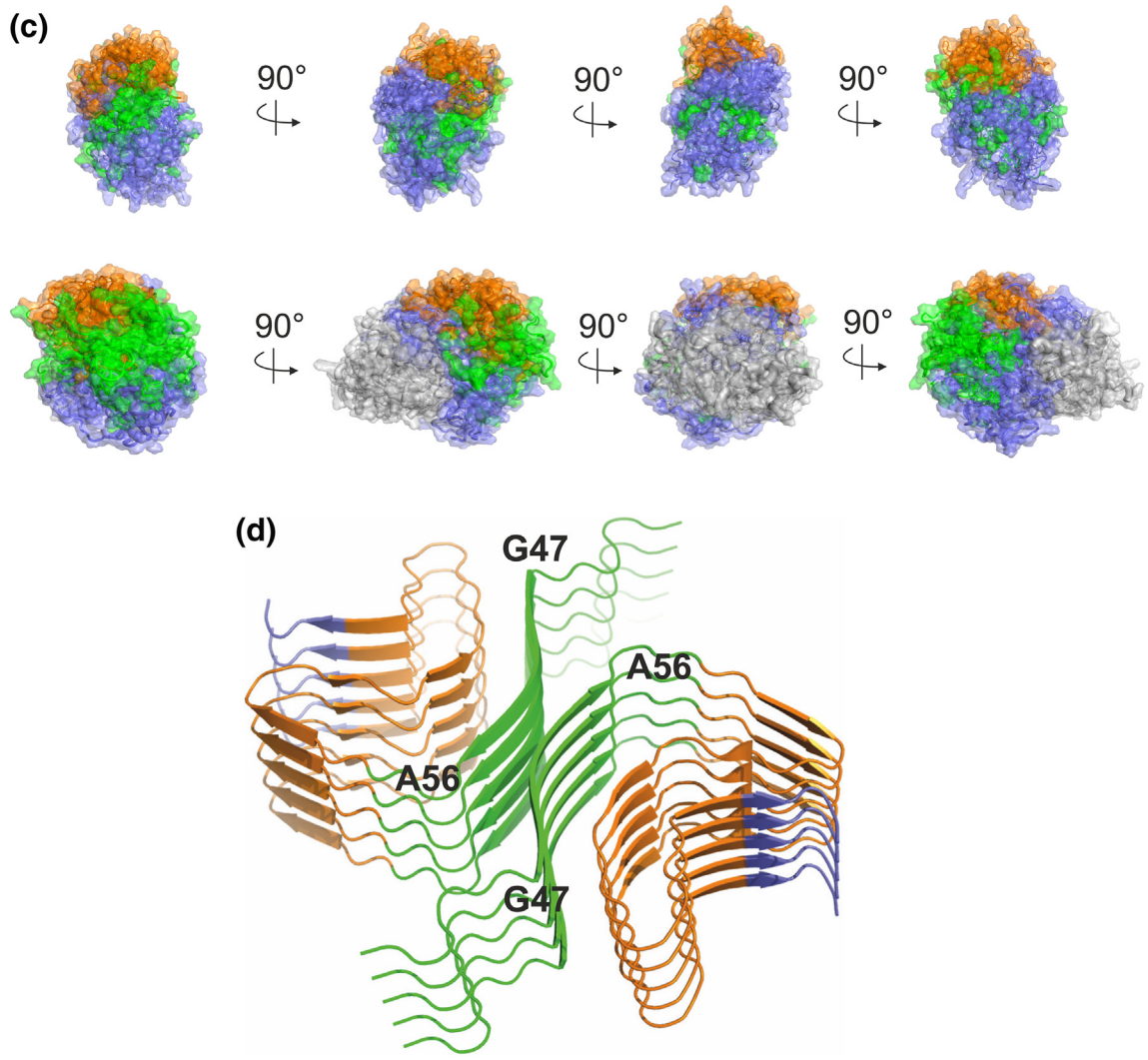

Fig. 5. (*continued*).

and represent NAC core-shielding interactions [22,23,28]. However, these contacts were observable for only less than 5% of the calculated structure in the ensemble of the aSyn:SERF1a complex.

We supposed that the loss of these protective contacts led to the exposure of amyloidogenic surfaces. To substantiate this assumption, we calculated the residue-specific surface accessibility of the ensemble by counting the number of hetero atoms within a 15 Å radius (Fig. 5B). We measured an increased neighboring atom number at the C-terminus of bound aSyn (aa 100–140) due to direct contacts with SERF1a, reflecting a decreased surface accessibility of this stretch. However, a decreased neighboring atom number was observable between residues 30–60, pointing towards an increased exposure of this region in the aSyn:SERF1a complex.

Superimposed lowest-energy structures (Fig. 5C), which reflect most probable orientations in the ensemble, describe how the exposure of residues 30–60 changes from non-contiguous patches with minor surface accessibility in free aSyn to a highly extended and solvent-protruding surface in the bound state, supporting this region's preferential deprotection. The exposed surface largely overlaps with segment $_{47}$GVVHGVTTVA$_{56}$, referred to as preNAC [18–20], which in the amyloid structure of aSyn corresponds to the outer N-terminal chain of the NAC beta-sheet core (Fig. 5D) [17–19]. Of particular relevance, preNAC is minimal a structural element of amyloid nucleation. It is able to separately polymerize into a beta sheet steric zipper [20], and it constitutes one of two known dimerisation interfaces by which separate protofibrils can respectively assemble into two distinct fibril polymorphs [19].

Remarkably, residues 61–96, which encompass the second dimerisation interface $_{68}$GAVVTGVTVA$_{78}$ as well as the central beta-arch core of the NAC [19], were less affected, as deduced by nearly unchanged heteroatom counting values (Fig. 5B). These results emphasize that SERF1a does not induce a complete deprotection of the amyloidogenic NAC region, but rather the specific exposure of one fibril-organizing element.

Discussion

By elucidating the amyloid-promoting mechanism of SERF1a, we have discovered that the pair of intrinsically disordered proteins SERF1a and aSyn retains a surprisingly high level of conformational freedom in complex, accounting for an extremely disordered, weak and transient interaction *in vitro* and in the cell. Consequently, the aSyn:SERF1a complex can be best represented by an ensemble of conformationally fluctuating states devoid of any stable secondary structure. The interaction leads to tertiary rearrangements that partially uncover a minimal amyloidogenic element of the NAC without inducing a stably folded structure. These rearrangements are sufficient to increase the amyloid polymerization tendency of complexed aSyn.

The aSyn:SERF1a interaction is close to random fuzziness, a to date only sporadically observed extreme manifestation of structural disorder [1]. IDPs undergoing a random fuzzy interaction form structurally disorganized complexes -in sharp contradiction to the traditional structure–function concept. Case-by-case as well as bioinformatics analyses have reported the existence in different organisms of unstructured protein homodimers/oligomers, as well as random fuzziness between one folded and one completely flexible protein partner [29–34]. The IDP pair prothymosin-α and histone H1.0 [2] provides a prototypic representation of a heterotypic random fuzzy protein–protein interaction. The two proteins form a physiologically active complex while both remaining unstructured and conformationally highly dynamic. Although the aSyn:SERF1a complex is similar in terms of extreme structural disorder, the mode of interaction differs substantially. Firstly, specific binding of aSyn to SERF1a derives from a defined linear stretch of charged residues, whereas widely distributed, interchanging contacts are established for the protyhmosin-alpha:H1.0 complex. Secondly, the interaction site is strongly sensitive to net charge modifications (*e.g.* phosphorylation), suggesting a tuneable binding mechanism. Thirdly, the binding mode accounts for a substantially weaker binding affinity (low micromolar *vs.* picomolar K_D of protyhmosin-alpha:H1.0 [2]). Moreover, SERF1a fundamentally differs from traditional amyloid modifying proteins, such as the well-analyzed molecular chaperone hsp90 [35,36]. This molecule i) interacts with intrinsically disordered substrates (*e.g.* aSyn or tau) *via* multiple hydrophobic patches that can give rise to large contact areas (up to 106 A for tau), ii) covers their aggregation-prone region, and iii) significantly reduces their overall flexibility in complex. Instead, the interaction between SERF1a and aSyn i) is specifically governed by charge and selectively restricted to one linear motif ii) leaves the aggregation-prone region exposed, and iii) does not reduce the flexibility of the interacting partners. From these considerations, we can principally deduce that random fuzziness can prime a structurally tightly organized and complex molecular process such as amyloid polymerization.

The transient and spatially restricted character of the aSyn:SERF1a interaction presents some conceptual homologies to weak and short lived protein complexes typical of dynamic membraneless cellular bodies. Though aggregation-prone, these complexes can become highly concentrated as long as they remain spatially and temporally controllable [37–39,44–46]. By similarity, the highly disordered aSyn:SERF1a association is reversible, weak, transient, and localized to intracellular bodies of non-amyloid nature. We suppose that the confined accumulation of aSyn and SERF1a into cytosolic bodies can easily rise the proteins' local concentrations well above total estimated values of and 5–10 μM and 2–4 μM, respectively (see supplementary material), conferring a physical significance to the low affinity of the interaction.

We finally speculate that an unnatural pathologic trigger can alter the dynamics of the complex. The increased binding affinity of pSer129-aSyn, which is a disease-associated modification [40], might for instance lead to an association/dissociation imbalance forcing the prolonged persistence of the complex in an amyloidogenic state.

Methods

All animal experiments were carried out in accordance with the guidelines and regulation of the Austrian Ministry of Research, Science and Economics. All experimental protocols were approved by the Austrian Ministry for Research, Science and Economics and by the local facility for animal experiments, Medical University of Graz, Institute for Biomedical Research, Graz, Austria.

Unless otherwise specified, all reagents were obtained from Sigma-Aldrich, Vienna, Austria.

High purity FITC-labeled aSyn C-terminal peptide GILEDMPVDPDNEAYEMPSEEGYQDYEPEA (FITC-aSynC) corresponding to amino acids 111–140 and the Ser129-phosphorylated variant GILEDMPVDPDNEAYEMP(pS) EEGYQDYEPEA (FITC-aSynC-pSer129) were purchased from Pepnome Inc. (Hong Kong, China).

Plasmids, constructs and mutagenesis

For recombinant protein expression in *E. coli*, the pRECEIVER-B02/*SERF1A* gene construct (GenBank: AF073518.1; clone no. EX-S0127-B2; SourceBiosciences Lifesciences, Nottingham, UK), and a pRSETB/*SNCA* gene construct (donation of Roberto Cappai, Melbourne, Australia) were used. For mammalian cell expression, the *SERF1a* gene was amplified using pRECEIVER-B02/*SERF1A* as a template, and cloned into the pEGFP-C2 vector (Clontech, Mountain View, CA) at the EcoRI/BamHI insertion sites. The resulting construct pEGFP/*SERF1a* was used for transfection and for mutagenesis. The pcDNA/*mCherry-SERF1a* construct was a gift from Ellen Nollen, Groningen, The Netherlands).

EGFP-alphasynuclein-WT was a gift from David Rubinsztein (Addgene plasmid #40822) [41].

SERF1a or aSyn single-point mutants were generated by site-directed mutagenesis according to the QuickChange II mutagenesis kit manual (Agilent, Santa Clara, CA). Mutagenesis templates for the expression in *E. coli* were pRECEIVER-B02/*SERF1A* and pRSETB/*SNCA*. Mutagenesis templates for mammalian expression were pEGFP/*SERF1a* and pcDNA/*mCherry-SERF1a.* See Table S1 for a comprehensive list of mutagenesis primers.

Fluorescence imaging in living cells

SH-SY5Y neuroblastoma cells (LGC Standards, Wesel, Germany) were grown at 37 °C and 5% CO_2 in DMEM/F-12 HAM medium supplemented with 10% FCS and penicillin/streptomycin antibiotics (PAA, Pasching, Austria). Cells were grown on 35 mm poly-D-lysine coated glass bottom dishes (MatTek, Ashland, MA) and transiently (co)-transfected with the constructs *EGFP-alphasynuclein-WT* and pcDNA/*mCherry-SERF1a* or pcDNA/*mCherry-K17E* using SuperFect transfection reagent (Qiagen, Hilden, Germany) according to the manufacturer's manual. DIC and fluorescence microscopy images were recorded on a Zeiss Observer Z1 microscope (Zeiss, Jena, Germany). Images were processed using ImageJ.

Immunoprecipitation from mouse brain extracts

The adult 2 months old C57BL/6 mouse were narcotized and sacrificed by intraperitoneal injection of thiopental (Sandoz, 250 mg/ml). The calvaria were opened and ipsilateral and contralateral cortex was harvested. For immunohistochemical analysis of cerebral tissue, the thorax was opened and the still beating heart was exposed. The animal was transcardially perfused (*via* left chamber) with a perfusion solution (4% paraformaldehyde +1% picric acid). After overnight fixation at +4 °C, the whole brain was harvested and embedded into paraffin-blocks for further investigations.

Cerebral tissue (0.5 g) was gently homogenized with a tissue grinder in 2 ml 50 mM Tris, 50 mM NaCl, 1% Octylphenoxy poly(ethyleneoxy)ethanol (IGEPAL CA-630), pH 7.4 supplemented with PhosStop phosphatase inhibitor; Protease-Inhibitor Mix HP, and 0.5% PMSF (lysis buffer), and centrifuged 10′ at 14,000*g*. The supernatant was pre-cleared for 1 h (Preclearing Matrix B-goat; Santa Cruz). 1 ml lysate was incubated overnight in the absence (control-IP) and in the presence of 1 µg anti-SERF1a IgG (clone K-13, Santa Cruz), respectively, on a rotary shaker. After the addition of ImmunoCruz IP/WB Optima B immunoprecipitation matrix (Santa Cruz), samples were further incubated for 1 h, centrifuged at 14,000*g* for 30″, and washed once with lysis buffer. Samples were split equally and washed twice with low salt buffer (lysis buffer with 50 mM NaCl) or physiologic salt buffer (lysis buffer with 150 mM NaCl), respectively. Beads were resuspended in denaturing, non-reducing LDS buffer (Life Technologies, Carlsbad, CA). Samples were added 1 mM DTT immediately before running them on 4–12% NuPAGE gels (Life Technologies).

For immunoblotting, gels were transferred to an Amersham Protran nitrocellulose membrane. Membranes were incubated overnight (4 °C) in 5% skim milk/Tris-buffered saline;0.05% Tween20 (TBST), 3 mM NaN_3, and shaken for 2 h at RT with the respective primary antibody diluted in 1% skim milk/TBST, 3 mM NaN_3 (1:1000 anti-aSyn (clone 2B2D1; Santa-Cruz Biotech) and 1:2000 anti-SERF1a (clone K-13; Santa Cruz Biotech), and 1.5 h with HRP-conjugated secondary antibody in 1% skim milk/TBST, 3 mM NaN_3 (1:2000 goat anti mouse (Santa Cruz Biotech) for aSyn and 1:2000 mouse anti goat (Santa Cruz Biotech) for SERF1a). The blots were then incubated with ECL reagent (Santa Cruz Biotech), and developed on a Kodak X-OMATIC film.

Immunofluorescence Staining (IF) on Paraffin-Embedded mouse brain sections

The following primary antibodies were used for IF staining: polyclonal goat anti-human SERF1a (K-13), IgG (Santa Cruz Biotechnology, Inc., TX, USA) and monoclonal mouse anti-human aSyn (2B2D1), IgG_1 (Santa

Cruz Biotechnology, Inc., TX, USA). FITC donkey anti-goat IgG (Santa Cruz Biotechnology, Inc., TX, USA) and rabbit anti-mouse Cy3 (Jackson ImmunoResearch Lab, Inc., West Grove, PA, USA) were used as secondary antibodies. All antibodies were diluted with Dako Cytomation Antibody Diluent with Background Reducing Components (Dako, Inc., Carpinteria, CA, USA).

Studies were carried out on 4% paraformaldehyde (PFA) fixed, paraffin embedded adult 2 months old C57BL/6 mouse brain. Sections of 4 μm were deparaffinized in xylene, and rehydrated with decreasing concentrations of ethanol according to standard methods. Antigen retrieval was used for tissue sections submerged in 10 mM Sodium Citrate Buffer, 0.05% Tween 20, (pH 6.0) for 10 min in a domestic microwave oven. Slides were allowed to cool down for 45 min at room temperature before rinsing in wash buffer (TBST, pH 7.4). Sections were blocked with UV ultra-block for 7 min before primary antibodies incubation at 4 °C overnight (SERF1a at 2.67 μg/ml and aSyn at 2 μg/ml). All incubation steps were performed in a dark moist chamber at room temperature. After 5 min of TBST wash secondary antibodies were applied: donkey anti-goat FITC (green) 0.50 μg/ml; rabbit anti-mouse Cy3 (Red) 1.88 μg/ml for 30 min. After rinsing in TBST, DAPI (blue) 5 μg/ml (Life Technologies, NY, USA) was added to the slides for 20 min as a nuclei counter stain. Sections were rinsed again with TBST before mounting with Vectashield mounting medium (Vector Lab, Inc., Burlingame, CA, USA). To acquire and analyze computerized images of cells, a Leica DM4000 B microscope (Leica Cambridge Ltd) equipped with Leica DFC 320 Video camera (Leica Cambridge Ltd) was used.

ThioFlavin-S (ThS) stain on Paraffin-Embedded mouse brain sections

Studies were carried out on 4% PFA fixed, paraffin embedded WT adult C57BL/6 mouse brain. Sections of 4 μm were deparaffinized in xylene, and rehydrated with decreasing concentrations of ethanol according to standard methods. The sections were then stained with fresh, filtered, aqueous 1% ThS for 1 min and rinsed 2x each for 3 min with 80%, and 95% ethanol. The slides were then rinsed in distilled water before 4′,6-diamidin 2-phenyldiol (DAPI) 5 μg/ml (Life Technologies, NY, USA) was added to the slides for 20 min as a blue nuclear counter stain. Sections were rinsed again with distilled water before mounting with Vectashield mounting medium (Vector Lab).

Protein purification

SERF1a and aSyn wildtype and single-point mutants were heterologously expressed in *E. coli* grown in LB-medium, or in minimal medium supplemented with $(^{15}NH_4)_2SO_4$ and ^{13}C-glucose as sole nitrogen/carbon sources for isotope-labeling. All proteins were purified as described previously [5]. Cysteine-containing variants were purified under reducing conditions in the presence of 1 mM DTT.

NMR spectroscopy

NMR measurements were carried out on a Bruker Avance III 700-MHz spectrometer equipped with cryogenically cooled TCI probehead. If not specified elsewhere, experiments were recorded on a 100 μM uniformly ^{15}N/^{13}C-labeled sample of aSyn or SERF1a in 50 mM Bis(2-hydroxyethyl)amino-tris(hydroxy-methyl)methan (bis-Tris), 20 mM NaCl, 3 mM sodium azide, pH 6.8, which were previously dialyzed against the same buffer. Spectra were processed using NMRPipe [42] and analyzed with Sparky (T. D. Goddard and D. G. Kneller, SPARKY 3, University of California, San Francisco). $\{^1H\}$-^{15}N heteronuclear NOE data were measured at a 700-MHz proton Larmor frequency as described [14].

Paramagnetic spin labeling

For site-specific paramagnetic conjugation, single cysteine variants of aSyn (A18C, A76C, 141C) or SERF1a (S22C, S30C, S41C, S56C) were generated as described under subheading “plasmids, constructs and mutagenesis”. Purified samples were dissolved in 10 mM Tris(hydroxymethyl)-aminomethan (Tris) (pH 8), 100 μM NaCl and mixed with 10 M equivalents of 3-(2-iodacetoamido)-2,2,5,5,tetramethyl-1-pyrrolidinyloxy radical (iodacetamido-PROXYL) and left in the dark at RT for 4 h to react. In order to remove unreacted spin-label buffer was exchanged twice with 50 mM bis-Tris, 20 mM NaCl, 3 mM sodium azide, pH 6.8, using a G25 desalting column (GE Healthcare Life Sciences).

Spin-coupled paramagnetic relaxation enhancements

Paramagnetic relaxation enhancements (PREs) of site-specifically spin labeled aSyn or SERF1a cysteine variants were measured as a ratio of peak intensities I_{red}/I_{ox} from ^{1}H,^{15}N HSQC spectra before (paramagnetic/

oxidized) and after addition of 6 M equivalents of ascorbic acid (diamagnetic/reduced). PRE-derived distances were calibrated as described elsewhere [27]. Rotational correlation time (τ_c) of the spin-labels in the aSyn:SERF1a complex was estimated from R_1 and R_2 relaxation rates in the para- and diamagnetic state obtained for the single cysteine variants aSyn A18C and SERF1a S30C. Combinations of intramolecular and intermolecular PREs were recorded according to the scheme shown in Fig. S5.

Solvent paramagnetic relaxation enhancements

To obtain sPRE data of 100 μM uniformly $^{15}N/^{13}C$-labeled aSyn free and in complex with 160 μM SERF1 by NMR spectroscopy, we used a saturation-based approach as described previously [43,44]. Briefly, the R_1 relaxation rates are determined by a saturation-recovery scheme followed by $^{1}H,^{15}N$ HSQC read-out experiments. For proton saturation, a 7.5 ms ^{1}H trim pulse followed by a gradient was applied. Then, z-magnetization is build up during the recovery delay, ranging between several milliseconds up to several seconds. Iterating through the different recovery delays is done in an interleaved manner, and short and long delays were ordered in an alternating fashion. For every R_1 measurement at least 8 delay times were recorded and for error estimation, at least one delay time was recorded as a duplicate.

R_1 rates were measured after stepwise addition of relaxation-enhancing gadodiamide [Gd(DTPA-BMA), Omniscan] (from 1 mM to 5 mM). The sPRE was obtained as the average change of the proton R_1 rate per concentration of the paramagnetic agent. Recovery delays were shortened after each addition of Gd(DTPA-BMA), in order to still recover all NMR signals in the longest delay.

sPRE data were analyzed as follows: peak intensities were extracted using the nmrglue[https://doi.org/10.1007/s10858-013-9718-x] Python package and fitted to a mono-exponential build up curve using the SciPy python package and equation.

$$I(t) = -A \cdot e^{-R_1 * t} + C \tag{1}$$

where *I(t)* is the peak intensity of the saturation-recovery experiment, *t* is the recovery delay, *A* is the amplitude of the z-magnetization build-up, C is the plateau of the curve and R_1 is the longitudinal relaxation rate. Duplicate recovery delays were used to determine the error for the fitted rates R_1.

$$\varepsilon_{\text{exp}} = \sqrt{\frac{1}{2N} \cdot \sum_{i=1}^{N} \delta_i} \tag{2}$$

where *N* is the number of peaks in the spectrum, *i* is the index of the peak, and δ_i is the difference of the duplicates for the *i*-th peak. The error of the rates R_1 was then obtained using a Monte Carlo-type resampling strategy. The solvent PRE is then obtained by performing a weighted linear regression using equation

$$R_1(c) = sPRE \cdot c + R_1^0 \tag{3}$$

where *c* is the concentration of Omniscan, $R_1(c)$ is the fitted R_1 rate at the present of Omniscan with a concentration *c*, R^0_1 is the R_1 in the absence of Omniscan and solvent PRE is the slope and the desired solvent PRE value. For the weighted linear regression, the previously determined errors ΔR_1 for R_1 was used, and the error of the concentration *c* was neglected.

SAXS

All SAXS data were recorded on an in-house SAXS instrument (SAXSess mc^2, Anton Paar, Graz, Austria) equipped with a Kratky camera, a sealed X-ray tube source and a two-dimensional Princeton Instruments PI•SCX:4300 CCD detector (Roper Scientific, Planegg, Germany). The scattering patterns were measured with 180 min exposure times (1080 frames, each 10 s) for several solute concentrations in the range from 1 to 6.7 mg/ml. Radiation damage was excluded based on a comparison of individual frames of the 180-min exposures, where no changes were detected. A range of momentum transfer of $0.012 < s < 0.63$ Å-1 was covered ($s = 4\pi \sin(\theta)/\lambda$, where 2θ is the scattering angle and $\lambda = 1.5$ Å is the X-ray wavelength).

All SAXS data were analyzed with the package ATSAS (version 2.5). The data were processed with the SAXSQuant software (version 3.9), and desmeared using the programs GNOM [45] and GIFT [46]. The forward scattering, I(0), the radius of gyration, R_g, the maximum dimension, D_{max}, and the inter-atomic distance distribution functions, (P(R)), were computed with the program GNOM. The masses of the solutes

were evaluated by comparison of the forward scattering intensity with that of a human serum albumin reference solution (molecular mass 69 kDa) and using Porod's law.

Ensemble structure calculations

The pool of structures was calculated using a modified version of Aria1.2/CNS [27]. Distance restraints were derived from i) chemical shift perturbations (residues 113, 119, 121, 124–127, 129–130, 132, 137, 140 of aSyn and 4, 6, 8–16, 18–19, 22–23, 27–28 of SERF1a shift or broaden upon addition of SERF1a or aSyn and must therefore be in the interface), and ii) paramagnetic spin-labeling using several combinations of spin-labeled and isotopically labeled aSyn:SERF1a samples (Fig. S4). Backbone torsion angle restraints were obtained from chemical shifts of SERF1a using TALOS+ [47]. Three pools of structures with different 'compactness' were generated during a molecular dynamics and simulated annealing run using i) all restraints, ii) all restraints, but with lower force constant on the PRE-derived distance restraints, or iii) all restraints except PRE-derived distance restraints. The final structures were refined in a shell of water molecules [48]. A total number of 30,000 structures (3 × 10,000) was generated and used as pool for further EOM analysis. For EOM analysis we used the built-in genetic algorithm and default settings. A subset of a few independent structures was selected by the algorithm which best describes the experimental SAXS, and used to prepare the figures showing R_g/D_{max} distributions.

To obtain an additional measure for the structure and compactness of aSyn in the absence and presence of SERF1a, the number of neighboring hetero atoms was computed for every atom of aSyn. To this end, all distances between a given atom of aSyn and all other hetero atoms were computed and the number of hetero atoms closer than 15 Å was counted. Next, a mean value for every residue was obtained by averaging the previously computed neighbor atom count across all atoms of the residue. This procedure was performed for every structure in both ensembles of aSyn (in the absence and presence of SERF1a), and the neighbor atom count of every residue was averaged over all 10,000 structures of the ensembles.

Circular dichroism spectroscopy

10 μM SERF1a, 10 μM aSyn or an equimolar mixture of both proteins were dialyzed against 20 mM NaPi, 50 mM NaF, pH 7.0. Far-UV-circular dichroism spectra of each solution were recorded at 25 °C on a J-715 spectropolarimeter (Jasco, Tokyo, Japan) between 195 nm and 250 nm, with a response time of 4 s and with a data point resolution of 0.2 nm using a 1 mm quartz cuvette. Each curve is the average of three independent accumulations.

Fluorescence anisotropy titrations

The fluorescence anisotropy of a 200 nM FITC-aSynC or FITC-aSynC-pSer129 solution in 50 mM (bis-Tris), 50 mM NaCl, 3 mM NaN_3, pH 6.8, was measured at 25 °C on a LB50 spectrofluorimeter equipped with excitation and emission polarizers (Perkin Elmer, Waltham, MA), at an emission wavelength of 525 nm upon excitation at 495 nm. Slits widths were 5 nm and 10 nm for excitation and emission, respectively. The fluorescence anisotropy is defined as [49].

$$r = (I_{VV} - G \times I_{VH})/(I_{VV} + 2G \times I_{VH}); -0.2 \leq r \leq 0.4 \quad (4)$$

where I_{VV} is the fluorescence intensity recorded with excitation and emission polarizers in vertical positions, and I_{VH} is the fluorescence intensity recorded with the emission polarizer aligned in a horizontal position. The G factor is the ratio of the sensitivities of the detection system for vertically and horizontally polarized light $G = I_{HV}/I_{HH}$.

Unless specified, binding curves were measured at low ionic strength (50 mM NaCl) for improving the saturation of weak binding mutants. FITC-aSynC was titrated against increasing amounts of different SERF1a variants previously dialyzed against the same buffer. FITC-aSynC-pSer129 was titrated against a previously dialyzed solution of wild-type SERF1a. For each point, the anisotropy was recorded over 30 s and the mean r values for each measurement were used. Anisotropy changes were fitted by using the Levenberg–Marquardt algorithm to the equation

$$r = \Delta r_{max} \frac{K_D + [SERF1a] + [FITCpep] - \sqrt{\left(K_D + [SERF1a] + [FITCpep]^2\right) - 4[SERF1a][FITCpep]}}{2[SERF1a]}. \quad (5)$$

where r is the observed anisotropy, Δr_{max} is the maximal anisotropy change, and K_D is the dissociation constant. *SERF1a* stands for wild-type SERF1a or any point-mutant. *FITCpep* stands for FITC-aSynC or FITC-aSynC-pSer129.

Accession numbers

UniProt accession numbers: O75920–2 for SERF1a; P37840 for aSyn.

Acknowledgements

This work was supported by the Austrian Science Fund (Project no. P22400 to S.F.F., P28854, W1226-B18, and I3792 to T.M.), the Austrian Research Promotion Agency (FFG: 864690 to T. M.) the Omics Center Graz (T.M.), the Integrative Metabolism Research Center Graz, the Austrian infrastructure program 2016/2017, BioTechMed/ Graz, the Bavarian State Ministry of Sciences, Research and the Arts (Bavarian Molecular Biosystems Research Network to T.M.), the Deutsche Forschungsgemeinschaft (Emmy Noether program MA 5703/1-1 to T.M.), the President's International Fellowship Initiative of CAS (No.2015VBB045 to T. M.), and the National Natural Science Foundation of China (No. 31450110423 to T.M.). E.S. thanks the Austrian Academy of Sciences for a DOCfFORTE fellowship.

Competing interests

The authors declare no competing financial interest.

Author contributions statement

T.M. performed SAXS measurements, data analysis, and ensemble structure calculations. T.M. and E.S. performed solvent-PRE measurements. D. A.M. and A.W. carried out molecular cloning and protein production. C.T.-A. prepared the cellular and brain tissue sections and performed immunofluorescence analysis. D.A.M., A.W., E.S., and S.L. prepared protein expression constructs. D.A.M. and A.W. performed protein purification. N.H.M. performed PRE-spin labeling, NMR measurement and data analysis, and PRE calculations. S.F.F. performed CD measurements, fluorescence anisotropy measurements, and immunoprecipitation analyses. S.F.F. and O.W. performed living cell fluorescence microscopy. C.H. performed neighboring heteroatom counting calculations. K.Z. provided technical NMR advice. A.J.K. provided cell culture access.

Appendix A. Supplementary data

Supplementary data to this article can be found online at https://doi.org/10.1016/j.jmb.2019.04.031.

Received 15 October 2018;
Received in revised form 17 April 2019;
Accepted 18 April 2019
Available online 26 April 2019

Keywords:
Fuzzy complexes;
Intrinsically disordered proteins;
Amyloids;
Alpha synuclein;
MOAG-4/SERF

Present address: Department of Internal Medicine, Division of Haematology, Medical University Graz, Auenbruggerplatz 38, 8036 Graz, Austria.

References

[1] M. Fuxreiter, Fuzziness in protein interactions-a historical perspective, J. Mol. Biol. 430 (2018) 2278–2287.
[2] A. Borgia, et al., Extreme disorder in an ultrahigh-affinity protein complex, Nature 555 (2018) 61–66.
[3] F.U. Hartl, Protein Misfolding diseases, Annu. Rev. Biochem. 86 (2017) 21–26.
[4] T.J. van Ham, et al., Identification of MOAG-4/SERF as a regulator of age-related proteotoxicity, Cell 142 (2010) 601–612.
[5] S.F. Falsone, et al., SERF protein is a direct modifier of amyloid fiber assembly, Cell Rep. 2 (2012) 358–371.
[6] J. Burré, et al., Alpha-synuclein promotes SNARE-complex assembly in vivo and in vitro, Science 329 (2010) 1663–1667.
[7] I. Alafuzoff, P. Hartikainen, Alpha-synucleinopathies, Handb. Clin. Neurol. 145 (2017) 339–353.
[8] K. Sugase, H.J. Dyson, P.E. Wright, Mechanism of coupled folding and binding of an intrinsically disordered protein, Nature 447 (2007) 1021–1025.
[9] N. Cremades, et al., Direct observation of the interconversion of normal and toxic forms of α-synuclein, Cell 149 (2012) 1048–1059.
[10] F.X. Theillet, et al., Structural disorder of monomeric α-synuclein persists in mammalian cells, Nature 530 (2016) 45–50.
[11] P. Tompa, Circular Dichroism in *Structure and function of intrinsically disordered proteins*, CRC Press, 2010 63–65.

[12] M. Kjaergaard, F.M. Poulsen, Disordered proteins studied by chemical shifts, Prog. Nucl. Magn. Reson. Spectrosc. 60 (2012) 42–51.
[13] J.A. Marsh, V.K. Singh, Z. Jia, J.D. Forman-Kay, Sensitivity of secondary structure propensities to sequence differences between alpha- and gamma-synuclein: implications for fibrillation, Protein Sci. 15 (2006) 2795–2804.
[14] N.A. Farrow, et al., Backbone dynamics of a free and phosphopeptide-complexed Src homology 2 domain studied by 15N NMR relaxation, Biochemistry 33 (1994) 5984–6003.
[15] Y. Yoshimura, et al., MOAG-4 promotes the aggregation of α-Synuclein by competing with self-protective electrostatic interactions, J. Biol. Chem. 292 (2017) 8269–8278.
[16] R. Sharma, Z. Raduly, M. Miskei, M. Fuxreiter, Fuzzy complexes: specific binding without complete folding, FEBS Lett. 589 (2015) 2533–2542.
[17] M.D. Tuttle, et al., Solid-state NMR structure of a pathogenic fibril of full-length human α-synuclein, Nat. Struct. Mol. Biol. 23 (2016) 409–415.
[18] R. Guerrero-Ferreira, et al., Cryo-EM structure of alpha-synuclein fibrils, Elife **7** (2018) pii: e36402.
[19] B. Li, et al., Cryo-EM of full-length α-synuclein reveals fibril polymorphs with a common structural kernel, Nat. Commun. 9 (3609) (2018).
[20] J.A. Rodriguez, et al., Structure of the toxic core of α-synuclein from invisible crystals, Nature 525 (2015) 486–490.
[21] C.O. Fernández, et al., NMR of alpha-synuclein-polyamine complexes elucidates the mechanism and kinetics of induced aggregation, EMBO J. 23 (2004) 2039–2046.
[22] C.W. Bertoncini, et al., Release of long-range tertiary interactions potentiates aggregation of natively unstructured alpha-synuclein, Proc. Natl. Acad. Sci. U. S. A. 102 (2005) 1430–1435.
[23] M.M. Dedmon, K. Lindorff-Larsen, J. Christodoulou, M. Vendruscolo, C.M. Dobson, Mapping long-range interactions in alpha-synuclein using spin-label NMR and ensemble molecular dynamics simulations, J. Am. Chem. Soc. 127 (2005) 476–477.
[24] P. Bernado, E. Mylonas, M.V. Petoukhov, M. Blackledge, D.I. Svergun, Structural characterization of flexible proteins using small-angle X-ray scattering, J. Am. Chem. Soc. 129 (2007) 5656–5664.
[25] C. Göbl, T. Madl, B. Simon, M. Sattler, NMR approaches for structural analysis of multidomain proteins and complexes in solution, Prog. Nucl. Magn. Reson. Spectrosc. 80 (2014) 26–63.
[26] J.R. Huang, et al., Transient electrostatic interactions dominate the conformational equilibrium sampled by multi-domain splicing factor U2AF65: a combined NMR and SAXS study, J. Am. Chem. Soc. 136 (2014) 7068–7076.
[27] B. Simon, T. Madl, C.D. Mackereth, M. Nilges, M. Sattler, An efficient protocol for NMR-spectroscopy-based structure determination of protein complexes in solution, Angew. Chem. Int. Ed. Engl. 49 (2010) 1967–1970.
[28] L. Salmon, et al., NMR characterization of long-range order in intrinsically disordered proteins, J. Am. Chem. Soc. 132 (2010) 8407–8418.
[29] J. Danielsson, et al., The intrinsically disordered RNR inhibitor Sml1 is a dynamic dimer, Biochemistry 47 (2008) 13428–13437.
[30] J.H. Fong, et al., Intrinsic disorder in protein interactions: insights from a comprehensive structural analysis, PLoS Comput. Biol. 5 (2009), e1000316. https://doi.org/10.1371/journal.pcbi1000316.
[31] M.S. Pometun, E.Y. Chekmenev, R.J. Wittebort, Quantitative observation of backbone disorder in native elastin, J. Biol. Chem. 279 (2004) 7982–7987.
[32] S.M. Simon, F.J. Sousa, R. Mohana-Borges, G.C. Walker, Regulation of Escherichia coli SOS mutagenesis by dimeric intrinsically disordered umuD gene products, Proc. Natl. Acad. Sci. U. S. A. 105 (2008) 1152–1157.
[33] T. Mittag, et al., Dynamic equilibrium engagement of a polyvalent ligand with a single-site receptor, Proc. Natl. Acad. Sci. U. S. A. 105 (2008) 17772–17777.
[34] O.S. Forsova, V.V. Zakharov, High-order oligomers of intrinsically disordered brain proteins BASP1 and GAP-43 preserve the structural disorder, FEBS J. 283 (2016) 1550–1569.
[35] G.E. Karagöz, et al., Hsp90-tau complex reveals molecular basis for specificity in chaperone action, Cell 156 (2014) 963-794.
[36] S.F. Falsone, A.J. Kungl, A. Rek, R. Cappai, K. Zangger, The molecular chaperone Hsp90 modulates intermediate steps of amyloid assembly of the Parkinson-related protein alpha-synuclein, J. Biol. Chem. 284 (2009) 31190–31199.
[37] S.K. Maji, et al., Functional amyloids as natural storage of peptide hormones in pituitary secretory granules, Science 325 (2009) 328–332.
[38] A. Patel, et al., A liquid-to-solid phase transition of the ALS protein FUS accelerated by disease mutation, Cell 162 (2015) 1066–1077.
[39] A. Molliex, et al., Phase separation by low complexity domains promotes stress granule assembly and drives pathological fibrillization, Cell 163 (2015) 123–133.
[40] J.P. Anderson, et al., Phosphorylation of Ser-129 is the dominant pathological modification of alpha-synuclein in familial and sporadic Lewy body disease, J. Biol. Chem. 28 (2006) 29739–52972.
[41] R.A. Furlong, Y. Narain, J. Rankin, A. Wyttenbach, D.C. Rubinsztein, Alpha-synuclein overexpression promotes aggregation of mutant huntingtin, Biochem. J. 346 (2000) 577–581.
[42] F. Delaglio, et al., NMRPipe: a multidimensional spectral processing system based on UNIX pipes, J. Biomol. NMR 6 (277–293) (1995).
[43] C. Hartlmüller, C. Göbl, T. Madl, Prediction of protein structure using surface accessibility data, Angew. Chem. Int. Ed. Engl. 55 (2016) 11970–11974.
[44] T. Madl, W. Bermel, K. Zangger, Use of relaxation enhancements in a paramagnetic environment for the structure determination of proteins using NMR spectroscopy, Angew. Chem. Int. Ed. Engl. 48 (2009) 8259–8262.
[45] D. Svergun, Determination of the regularization parameter in indirect-transform methods using perceptual criteria, J. Appl. Crystallogr. 25 (1992) 495–503.
[46] A. Bergmann, G. Fritz, O. Glatter, Solving the generalized indirect Fourier transformation (GIFT) by Boltzmann simplex simulated annealing (BSSA), J. Appl. Crystallogr. 33 (2000) 1212–1216.
[47] Y. Shen, F. Delaglio, G. Cornilescu, A. Bax, TALOS+: a hybrid method for predicting protein backbone torsion angles from NMR chemical shifts, J. Biomol. NMR 44 (2009) 213–223.
[48] J.P. Linge, M.A. Williams, C.A. Spronk, A.M. Bonvin, M. Nilges, Refinement of protein structures in explicit solvent, Proteins 50 (2003) 496–506.
[49] J.R. Lakowicz, Principles of Fluorescence Spectroscopy, Kluwer Academic Press, 1999.
[50] D.W.A. Buchan, F. Minneci, T.C.O. Nugent, K. Bryson, D.T. Jones, Scalable web services for the PSIPRED protein analysis workbench, Nucleic Acids Res. 41 (2013) W349–W357.